

Millimeter Wave Interferometry for Ejecta Concentration Measurements in Plume-Surface Interactions

Nicolas Rasmont¹, Hussein T. Al-Rashdan², Gregory S. Elliott³, Joshua L. Rovey⁴, and Laura Villafañe⁵
University of Illinois at Urbana-Champaign, Urbana IL, 61801

A novel method to measure the concentration of ejecta generated by the impingement of rocket plumes on granular surfaces is presented. This method is based on the principle of millimeter wave interferometry, using a fully-integrated frequency modulated continuous-wave 60-64 GHz radar to measure the path-integrated ejecta concentration between the radar itself and a reflector. The instrument is capable of quantitative measurements of high path-integrated ejecta concentrations up to 0.317 ± 0.133 vol%.m, one order of magnitude higher than state-of-the-art optical methods, at a repetition rate of 10 kHz and independently of the particle size distribution of the material. The interferometer was calibrated using a particle shadow counting technique for path-integrated concentrations up to 0.0223 ± 0.0008 vol%.m ($0.280 \pm 0.010 \times 10^9$ particles.m⁻²) and demonstrated on a reduced-scale plume-surface interaction experiment using a 6.5 N cold gas thruster impinging on a bed of regolith simulant under lunar (6.67 Pa) and martian (800 Pa) ambient pressures. A glass microsphere regolith simulant with a mean particle diameter of 105 μ m and a standard deviation of 17 μ m was used for calibration and demonstration. The instrument performed nominally in both demonstrations conditions, measuring a maximum path-integrated ejecta concentration of 0.0419 ± 0.0170 vol%.m ($0.527 \pm 0.214 \times 10^9$ particles.m⁻²) in the lunar case and 0.131 ± 0.053 vol%.m ($1.65 \pm 0.67 \times 10^9$ particles.m⁻²) in the martian case.

I. Introduction

PLUME-Surface Interactions (PSI) have been identified as a major challenge to current and future exploration programs of the Moon, Mars, and other rocky bodies of the solar system. Supersonic ejecta generated during the descent and landing of a spacecraft on the Moon can cause significant damage to any nearby infrastructure, in addition to blinding and contaminating the spacecraft [1–3]. The formation of deep craters capable of toppling the spacecraft has also been identified as a concern for martian landings [4, 5]. The ability to predict the cratering, flow and particle dynamics characteristic of PSI under different conditions is hindered by their coupled nature, the spatial coexistence of very different flow regimes with a wide range of particle loading, and their unsteady behavior. Knudsen and Mach numbers vary from subsonic to supersonic rarefied conditions between the nozzle exit and the surface, within a particle-laden flow that itself ranges from dilute to very densely loaded. Different erosion mechanisms have been identified that may dominate at different temporal stages during impingement depending on flow and particle parameters. There is a growing need for experimental datasets that can be used to better understand the emerging fluid-particle-surface interactions and to benchmark and validate PSI predictions. Given the high speeds and optically dense particle-laden flow near impingement, new diagnostics are needed for ground PSI experiments as well as for flight instruments. The development of techniques capable of reconstructing the concentration of the landing ejecta cloud is an important objective of current PSI studies[6]. Previous works by Lane and Metzger used optical techniques to measure the number density of a lunar landing ejecta cloud through optical extinction [7, 8] or particle side-scattering [9], both of which can be related to concentrations by the Beer-Lambert law. However, this process requires the local particle size distribution of the ejecta cloud to be measured or estimated, which presents a significant experimental challenge when landing on a poorly characterized soil or if the particles become spatially segregated by size. Furthermore, at length scales relevant to PSI experiments ($\sim 1 - 10$ meters), optical transmission rapidly falls to zero for number concentrations higher than 10^{10} m^{-3} and particle diameters larger than 10 μ m [8], which restricts optical techniques to the relatively narrow case of low concentrations of finely grained ejecta.

¹PhD Candidate, Department of Aerospace Engineering, 324 Talbot Laboratory, 104 South Wright St, AIAA Student member.

²PhD Candidate, Department of Aerospace Engineering, 324 Talbot Laboratory, 104 South Wright St, AIAA Student Member.

³Professor, Department of Aerospace Engineering, 301 Talbot Laboratory, 104 South Wright St, AIAA Associate Fellow.

⁴Associate Professor, Department of Aerospace Engineering, 317 Talbot Laboratory, 104 South Wright St, AIAA Associate Fellow.

⁵Assistant Professor, Department of Aerospace Engineering, 313 Talbot Laboratory, 104 South Wright St, AIAA Member.

A novel method capable of addressing the challenges present in high loading environments with relatively large particles is proposed and demonstrated in this study. It is based on the principle of millimeter-wave (mmWave) interferometry, which has been extensively investigated for medical [10–13] and industrial [14–18] purposes, and is a well established method to measure electron densities in plasma devices [19–22]. A fully integrated, frequency modulated continuous-wave (FMCW) radar operating between 60 and 64 GHz illuminates the area-under-test (AUT), tracking the phase shift of the signal bouncing off a reflector located at a known position. The FMCW mode of operation allows the interferometer to discriminate between the reflector echo and the AUT clutter without requiring the large and complex quasi-optical beam forming system of purely continuous-wave interferometers [23, 24]. The phase measurements provide the concentration of ejecta integrated along the line of sight between the radar and the reflector with a repetition rate of 10 kHz, independently of the size distribution of the material, for a range of concentrations at least one order of magnitude higher than optical techniques.

II. System Concept

The operating principle of mmWave interferometry consists in measuring small changes in the time-of-flight (TOF) τ of a mmWave beam propagating between an emitter (TX) and a receiver (RX) by tracking the phase shift between the signals received and sent over time. τ depends on the speed of light in vacuum c_0 and on the dielectric constant of the medium ϵ_m along the propagation path of the wave $l_{TX,RX}$, as provided by Eq. (1):

$$\tau = \int_{TX}^{RX} \frac{\sqrt{\epsilon_m}}{c_0} dl \quad (1)$$

Suspended particles will modify the dielectric properties of the propagation medium, in our case air or a reduced nitrogen atmosphere. The effective dielectric constant ϵ_{eff} of a particle-medium mixture, such as an ejecta cloud, is given by the Maxwell-Garnett formula [25] as a function of the volume fraction of ejecta δ , the dielectric constants of the medium ϵ_m , and the dielectric constant of the ejecta material ϵ_e , Eq. (2):

$$\sqrt{\epsilon_{\text{eff}}} = \sqrt{\epsilon_m} \left(1 + \frac{3\delta}{2} \left(\frac{\epsilon_e - \epsilon_m}{\epsilon_e + 2\epsilon_m} \right) \right) \quad (2)$$

The Maxwell-Garnett formula requires the volume fraction of ejecta in the medium to be much smaller than unity ($\delta \lesssim 1\%$), which is valid for current PSI observations reported in the literature [2]. Other effective medium theories, such as the Bruggeman mixing formula, are applicable for higher volume fractions. The phase shift $\Delta\phi$ of a wave with frequency f_0 due to the presence of ejecta on the propagation path is therefore:

$$\Delta\phi = 2\pi f_0 \Delta\tau = \frac{2\pi f_0}{c_0} \int_{TX}^{RX} \sqrt{\epsilon_{\text{eff}}} - \sqrt{\epsilon_m} dl = \frac{3\pi f_0}{c_0} \left(\frac{\epsilon_e - \epsilon_m}{\epsilon_e + 2\epsilon_m} \right) \int_{TX}^{RX} \delta dl \quad (3)$$

Equation (3) shows two remarkable properties of interferometric ejecta density measurements. They are linearly proportional to the path-integrated ejecta volume fraction, from which a tomographic reconstruction of the ejecta distribution can be created, and they are independent of the ejecta particle size distribution. This allows the instrument to provide a reliable measure of the volume fraction even if the ejecta density exceeds its initial calibration range or if a shift of the particle size distribution occurs in the measurement volume.

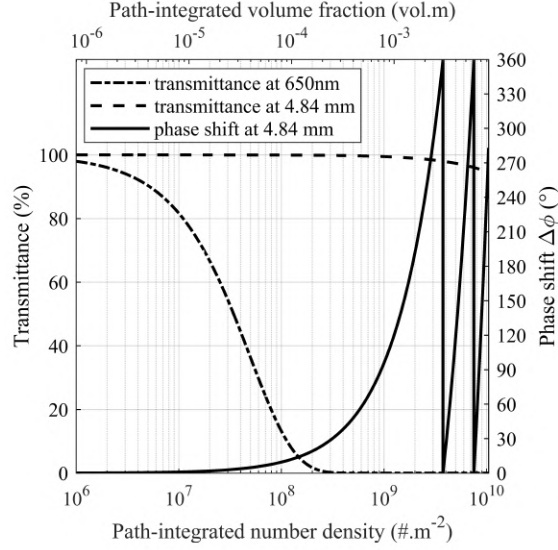


Fig. 1 Comparison of the attenuation and phase shift of 650 nm laser and 4.84 mm (62 GHz) beams travelling through monodisperse glass regolith simulant with a particle diameter of 105 μm .

Equation (3) can be used to compare the expected performances of optical attenuation and mmWave interferometry. Fig. 1 shows the attenuation of a 650 nm laser beam and the attenuation and phase shift of a 60 GHz wave travelling through various concentrations of monodisperse 105 μm glass regolith simulant, which is a representative simulant for Mars analog PSI experiments. Attenuation in the optical and mmWave range is estimated using the Beer-Lambert law, with extinction efficiencies calculated using Mie scattering theory, as provided by the software MiePlot [26]. It can be noticed that mmWave interferometry is capable of measuring ejecta concentrations one order of magnitude higher than a laser instrument if restricted to the $[0^\circ, 360^\circ]$ angular range. It can be extended to higher concentrations if phase unwrapping is used. Phase unwrapping is a class of signal processing techniques that allow the extraction from a quadrature signal of continuous phase traces with ranges greater than 360° by detecting and removing so-called "wrapping discontinuities" from the original phase signal. A lower operating frequency would also increase the upper measurement limit of the interferometer at the expense of the sensitivity of the system at lower concentrations, and vice-versa.

Attenuation by the ejecta particles is undesirable in mmWave interferometry as it reduces the signal-to-noise ratio (SNR). The wavelength of mmWaves is one to two orders of magnitude larger than the diameter of typical ejecta particles encountered in PSI. The mmWave-particle interaction therefore takes place in the Rayleigh scattering regime, with lower extinction efficiencies than in the geometric regime encountered by optical instruments. For a monodisperse 105 (μm) glass regolith simulant with a dielectric constant of 4.5, the Mie theory predicts that a mmWave beam with a wavelength of 5 mm will have an extinction efficiency twenty thousand times lower than a visible 650 nm beam, as shown in Fig. 2. Consequently, a mmWave beam experiences negligible extinctions for path-integrated volume fractions lower than 5 vol%.m. This value is well above the measurement range of the interferometer, as it would require the unwrapping of several hundreds consecutive phase jumps.

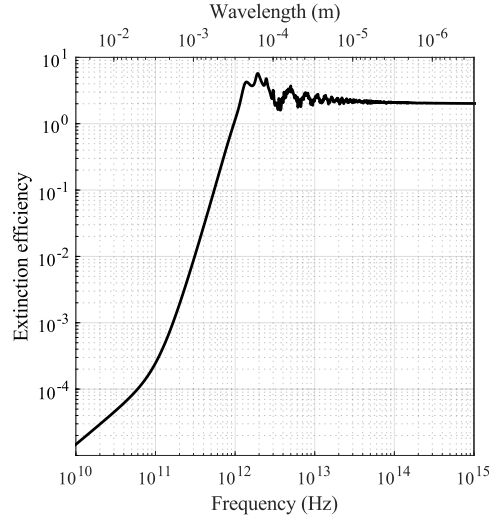


Fig. 2 Mie theory extinction efficiency of a $105\ \mu\text{m}$ glass particle as a function of the frequency and wavelength of the incoming electromagnetic wave obtained using the software MiePlot [26].

III. Experimental Setup

The mmWave interferometer was calibrated using a multi-elements slot funnel. The funnel elements were characterized by an optical particle counting method and combined to create a particle cloud with well-defined concentration and dimensions. Then, the interferometer was demonstrated in a PSI facility with environmental parameters relevant to martian and lunar landings.

A. Millimeter Wave Interferometer

The mmWave interferometer system is composed of two evaluation boards manufactured by Texas Instruments, the AWR6843ISK and DCA1000EVM, shown in Fig. 3. The AWR6843ISK carries a AWR6843[27] radar chip, which integrates a complete 60-64 GHz FMCW 3 TX, 4 RX radar transceiver with phase-locked loop (PLL), analog-to-digital converters (ADC), digital signal processing (DSP) module and microcontroller in a $10.4 \times 10.4\ \text{mm}$ package. The DCA1000EVM [28] is an interfacing board that captures the raw ADC data from the radar and streams it to a computer over a 1 GBps Ethernet link.

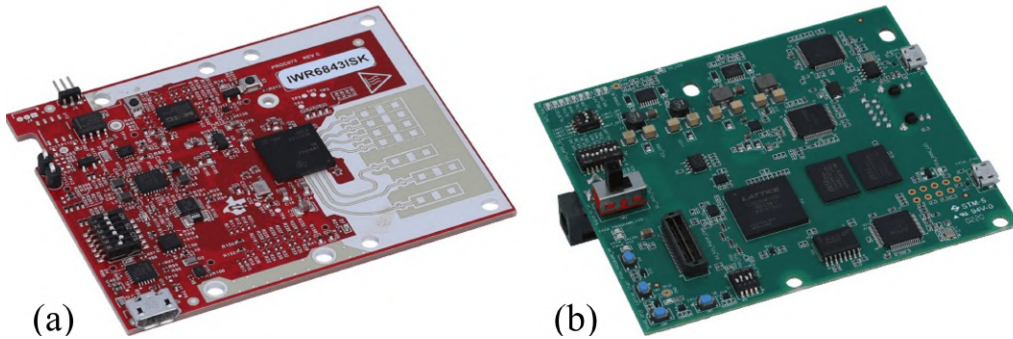


Fig. 3 Texas Instruments evaluation boards AWR6843ISK (a) and DCA1000EVM (b).

Fig. 4 shows the radar interferometer in its experimental configuration. The radar system is associated with a 31.75 mm diameter copper disk reflector, whose line of sight with the radar antenna defines the measurement chord of the interferometer. A planar reflector is used instead of a more conventional corner cube because its highly directional

cross-section reduces the effect of multipath interferences. Both components are mounted on optical posts with ball-and-socket joints for alignment purposes. The AWR6843ISK and DCA1000EVM are protected from the ejectas by a PLA and acrylic enclosure including a ultra-high molecular weight polyethylene (UHMWPE) window transparent to mmWaves.

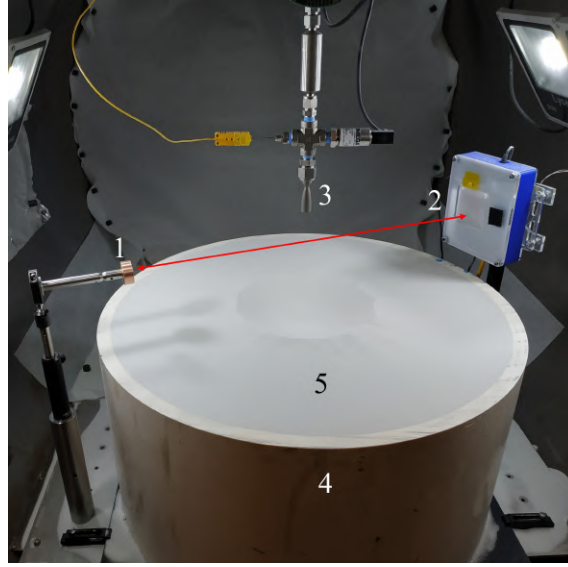


Fig. 4 Radar interferometer in experimental configuration, showing the planar reflector (1), radar system enclosure (2), thruster (3), particle bed (4), and granular surface (5).

The echo corresponding to the reflector is extracted from the radar range data and phase tracked between pulses, providing the interferometric phase shift measurement. The range bin corresponding to the reflector is identified by comparing the range data of the area under test with and without the reflector installed. In order to reject clutter and multipath interferences as efficiently as possible, it is desirable to use the largest chirp bandwidth B allowed by the radar system, which is $B = 4$ GHz. The chirp slope is set to its maximum value of $\frac{df}{dt} = 100$ MHz/ μ s, providing a chirp time $T = 40$ μ s which, combined with an idle time between chirp $t_{\text{idle}} = 60$ μ s, gives an acquisition rate $r = 10$ kHz. Improvements in the transfer speed to the computer, which is currently limited to half of its maximum bandwidth due to an impedance mismatch with the facility's Ethernet feedthrough, could increase the acquisition rate to 20 kHz, which is comparable to the acquisition rate of state-of-the-art high-speed cameras[29].

B. Calibration Setup

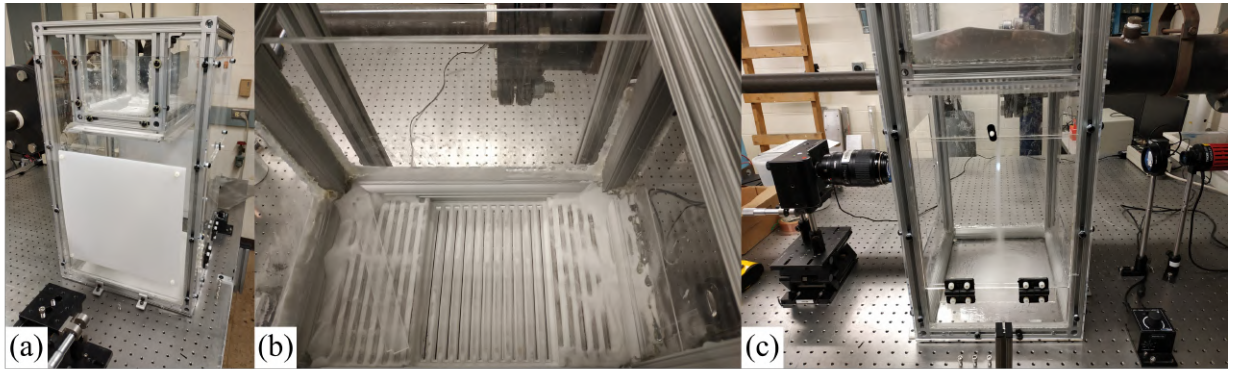


Fig. 5 Calibration rig (a), detail of the particle hopper slot array (b) with 12 slots open, and optical measurement of single-slot particle density (c).

The calibration approach is to acquire interferometric measurements for a cloud of particles with a known path-integrated density. This path-integrated density is determined using an optical method, which is the current state-of-the-art method for particle density measurements. High particle concentrations that would saturate any optical diagnostic, yet are within the measurement range of the interferometer, are characterized using a divide-and-conquer approach. First, optical particle-counting is used to accurately determine the particle density of a thin particle cloud. Then, a number of such individually-resolved clouds of known densities are combined to create a thicker particle cloud. The phase shift of the signal is then measured for clouds of different densities, therefore generating a calibration point for the instrument. We assume that, due to the almost completely vertical trajectory of the falling particles, the clouds do not have any interactions with each others. Therefore, the number densities of each cloud can be linearly added together.

A calibration rig, shown in Fig. 5, was designed and manufactured. It consists of a funnel assembly containing a particle hopper, a sliding trapdoor, and an array of 25 slots, each with a width of $600\ \mu\text{m}$, a length of $140\ \text{mm}$, and a spacing of $9.525\ \text{mm}$. An acrylic enclosure equipped with two UHMWPE windows encloses the area under the funnel to prevent particle egress. Each slot can be individually masked or opened, creating a curtain of falling particles sufficiently thin to be resolved by a shadowgraphic method. The shadowgraphic instrument is composed of a backilluminating $1.5\ \text{W}$ white LED collimated by a biconvex lens with a focal length of $100\ \text{mm}$. A $1.3\ \text{Megapixel}$ Chronos 1.4 high-speed camera equipped with a Canon EF $100\ \text{mm}$ macro lens is used for imaging the particle stream at 1057 frames per second. An exposure of $5\ \text{microseconds}$ is used to prevent motion blur of the falling particles, and a low aperture setting of $f/16$ is used to maximize the depth of field around the particle curtain. The images are then background-subtracted, segmented, and the particles counted using an algorithm implemented in MATLAB. The algorithm is adapted to resolve particles clusters, which otherwise can severely disturb state-of-the-art particle-counting algorithms, by taking the average particle area of a sample of well-resolved, unclustered particles using a Hough transform disk detector, as shown in Fig. 6. Then, the total apparent particle area of the segmented image is divided by this average particle area, providing the particle number density in the frame.

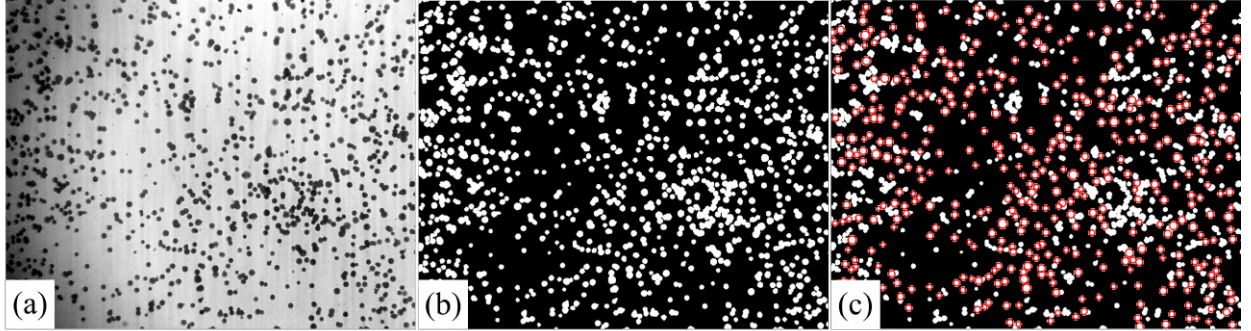


Fig. 6 Input image, (a), segmented image (b), and sampled particles (c) obtained during the particle counting process.

Once the particle density generated by a single slot is known, the radar phase shift caused by an increasing number of open slots, between 1 and 16, is measured. The calibration curve of the radar interferometer is generated using the assumption that the number density of each open slot can be linearly added together. The slope of this calibration curve is determined through the least-square linear regression of this dataset assuming a zero intercept term, as in Eq. (4):

$$\hat{\beta} = \frac{\sum_{i=1}^n y_i x_i}{\sum_{i=1}^n x_i^2} \quad (4)$$

The error on this slope is calculated using Eq. (5), assuming normally distributed error terms:

$$\sigma_{\hat{\beta}} = \sqrt{\frac{\frac{1}{n-2} \sum_{i=1}^n (y_i - \hat{y}_i)^2}{\sum_{i=1}^n (x_i - \hat{x}_i)^2}} \quad (5)$$

C. Plume Impingement Setup

PSI experiments are conducted at the University of Illinois at Urbana-Champaign (UIUC) in a 1.2-meter diameter by 2.1-meter long vacuum chamber with a total volume of 2375 liters, Fig. 7. The chamber, manufactured by the GNB Corporation, is equipped with a cart assembly integrating a 32" acrylic sheet that replaces the original door for improved optical access. In the new configuration the chamber is capable of a base pressure of 5 mTorr using a Kinney KT-150 roughing pump. A cylindrical bed made of PVC with a height of 12" and a diameter 24" contains the granular material, Fig. 8.

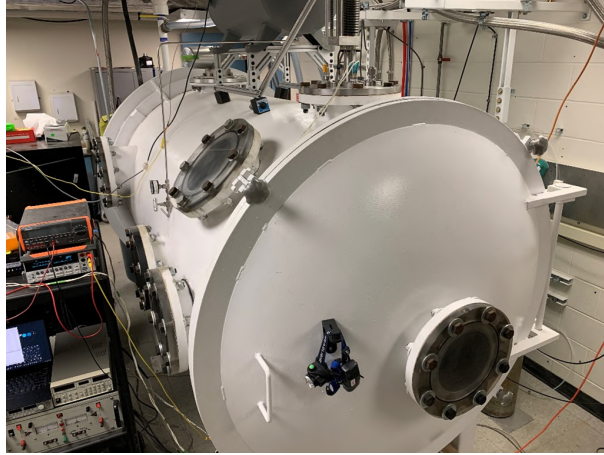


Fig. 7 Vacuum chamber housing the PSI facility.

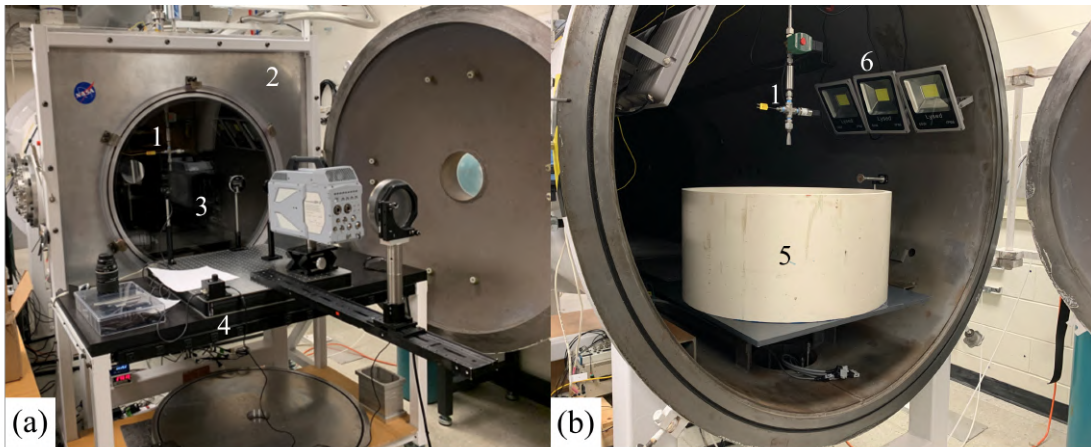


Fig. 8 Details of the optical access cart (a) and particle bed (b) used in the PSI facility. Thruster assembly (1), cart frame (2), acrylic window (3), optical table (4), granular media bed (5), internal LED lighting (6).

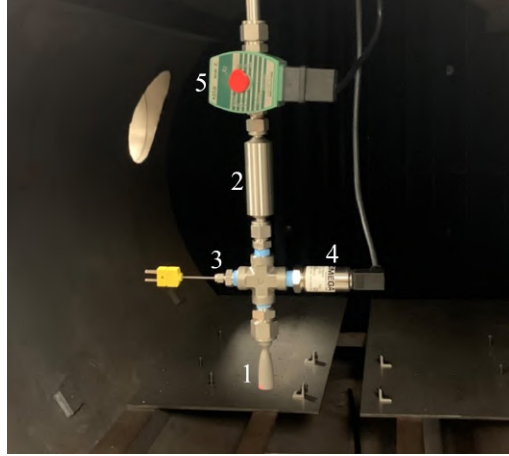


Fig. 9 6.5 N cold gas thruster used in the PSI facility. Nozzle (1), damping chamber (2), thermocouple (3), pressure sensor (4), solenoid valve (5).

The 6.5 N cold gas thruster used in this study, shown in Fig. 9, was previously described by Al-Rashdan [30] in their study of jet impingement on flat plates. It is located directly above the particle bed to simulate the operation of a retrograde rocket thruster impinging on a planetary surface. It integrates a 304 stainless steel Mach 5 bell nozzle with an exit diameter of 1 cm, a damping chamber, a thermocouple, a pressure sensor, and a fast solenoid valve that controls the incoming flow of nitrogen at 1.2 MPa and ambient temperature. Nitrogen was selected as the feed gas because of its ease of handling and its heat capacity, which is similar to the decomposition products of hydrazine. The thruster is fed by a 20-gallon reservoir tank through low coefficient of flow connectors, ensuring that the flow will not be choked upstream of the nozzle throat. The reservoir tank is periodically replenished from a commercial nitrogen cylinder with a purity of 99.999 %. The flow parameters for this thruster system and a representative landing thruster, the Aerojet MR-107-N used on the Phoenix mission, are reproduced in Tables 1 and 2, from Al-Rashdan [30]. The thruster is mounted on a bellowed linear stage with 15 cm of travel, allowing millimeter accuracy over the vertical position of the nozzle exit plane above the granular surface. The thruster fires in 1-second pulses in order to limit the drift in ambient pressure to $\Delta P = +150\text{Pa}$ during firing. The nearly-square stagnation pressure curve enabled by the thruster helps the replication of experimental conditions for validation and verification of numerical models.

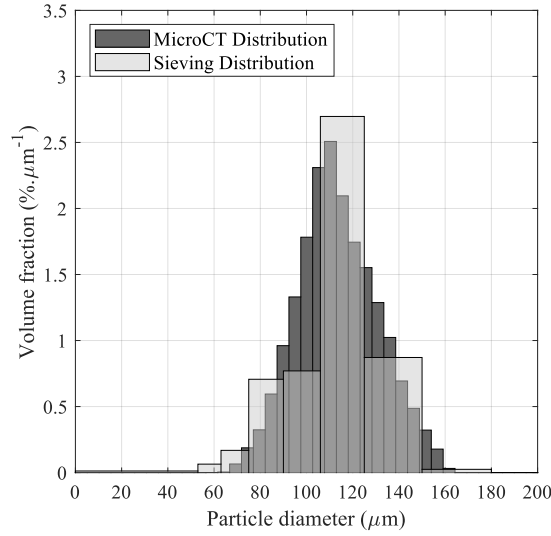
Table 1 Dimensional flow conditions of the thruster used in this study compared to the Aerojet MR-107-N.

Parameter	Current Thruster	MR-107-N
Chamber Pressure (MPa)	1.20	0.26-0.84
Exit Pressure (Pa)	2268.04	3240
Ambient Pressure (Pa)	6.7-800	0-858
Exit Velocity (m/s)	720.69	1929
Exit Temperature (K)	50	3300
Exit Viscosity (Pa-s)	$3.15 \cdot 10^{-6}$	$9.4 \cdot 10^{-6}$
Mean Free Path (μm)	0.517	6000
Mass Flow Rate (g/s)	8.65	320

Table 2 Non-dimensional flow conditions of the thruster compared to the Aerojet MR-107-N.

Parameter	Current Thruster	MR-107-N
Mach Number	5.0	4.7
Jet Pressure Ratio	2.84-340	3.8
Reynolds Number	$3.49 \cdot 10^5$	$3.4 \cdot 10^5$
Knudsen Number	$5.17 \cdot 10^{-5}$	0.03

The particles used as regolith simulant are Ballotini solid glass microspheres with a density $\rho = 2500 \text{ kg.m}^{-3}$ and a particle size distribution (PSD) with an average diameter $D = 105 \text{ }\mu\text{m}$ and a standard deviation $\sigma_D = 17 \text{ }\mu\text{m}$. These particles are typically used in industry as garnet in high-pressure waterjet cutting. A simulant with a relatively narrow size distribution was selected instead of a material more representative of martian or lunar regolith to simplify the PSI physics involved in our experiment. While the radar interferometer measures volume fractions, and is agnostic to the PSD (i.e. two ejecta clouds with the same volume fraction but differing particle size distributions have the same phase shift), it is calibrated against a particle cloud of known number density. The calibration process therefore requires the conversion of this number density (which the radar cannot measure directly) to a volume fraction (which the radar can measure directly). This conversion is made using an accurate measure of the particle size distribution. We measured the PSD by sieving, using a sieve shaker with size breaks at 53, 63, 90, 106, 125, 150, 180, 250, and $350 \text{ }\mu\text{m}$, and by X-ray microtomography images of particles samples obtained using a Zeiss Xradia Bio MicroCT imaging system. The tomographic images were segmented using a watershed algorithm implemented in MATLAB, resulting in a set of individually-labelled particles whose diameters were measured and binned to determine the PSD of the sample. The results of the two methods are shown in Fig. 10 and are in close agreement with each other and the specifications provided by the manufacturer.

**Fig. 10 Number-size distribution of the glass regolith simulant used as measured by computed microtomography and sieving.**

IV. Results

This section presents the results obtained during the calibration and demonstration of the radar interferometer in martian and lunar environments. The path-integrated ejecta density (PID) values are reported in the text in particles.m^{-2} , as it is the unit in which the radar was calibrated. Figures also report PID values as volume fraction ($\text{vol}\%.\text{m}$) based on the measured size distribution of the particles, with a proportionality ratio between the two units of $7.96 \times 10^{-11} \text{ }\%.\text{particle}^{-1}.\text{m}^3$. Path-integrated measurements may seem cumbersome and hard to interpret when

compared to path-averaged measurements. The first are chosen in this work to acknowledge the path-integrated nature of the results. Path-averaged measurements can be obtained by dividing by the length of the propagation path (58 cm for the present instrument), as in Eq. (6):

$$\bar{\delta} = \frac{1}{l_{TX,RX}} \int_{TX}^{RX} \delta dl \quad (6)$$

The ease of interpretation of path-averaged values is deceptive for a measurement technique that is inherently path-integrated. If the ejecta cloud is physically much smaller than the propagation path, as it is often the case in PSI experiments, the path-averaged density will be much lower than the actual cloud density. Therefore, unless a tomographic reconstruction is used to determine the spatial distribution of the particle density, or an estimate of the size of the ejecta cloud is obtained through another measurement method, we recommend and will use path-integrated values and units.

A. Radar calibration

Optical particle counting measurements provided a path-integrated density of $1.75 \pm 0.26 \times 10^7$ particles.m⁻² per funnel slot. Radar measurements were conducted up to 16 open slots, three times for each level. The results are presented in Fig. 11 with the zero-intercept calibration curve and its associated margin of error. The resulting calibration slope is $\beta = 9.03 \pm 2.66^\circ \cdot 10^{-8}$ particles⁻¹.m², with a coefficient of determination $r^2 = 0.9528$.

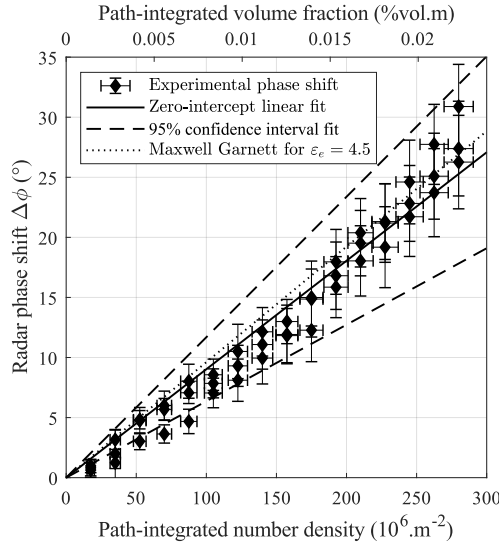


Fig. 11 Radar calibration data and linear fit along with theoretical Maxwell Garnett results for $\epsilon_e = 4.5$.

Also reported in Fig. 11 is the theoretical prediction of radar phase shift from the Maxwell-Garnett equation for a particle dielectric constant of 4.5, which is consistent with previous reports of borosilicate glass at microwave frequencies [31]. There is a close match between the experimental calibration and the theoretical curve, with a gap of only 6.4% between the two slopes. The dominant error source of this calibration procedure is aerodynamic perturbation of the particle curtain structure. A downdraft air current is created by the falling particles, with increasing intensity as more slots are concurrently open. This downdraft creates both a systematic bias and a random error term in the calibration. First, the downdraft locally reduces the pressure, which tends to contract the volume of each particle curtain, while the number of particles generated by each slot remains constant. Therefore, the particle density increases nonlinearly with the number of open slots, above the simple addition of each slot's contribution, leading to a systematic bias on the calibration. Secondly, the turbulence associated with the downdraft leads to particle density fluctuations over the course of each calibration measurement, which leads to the increasing random error term on the calibration observed in Fig. 11. Performing the calibration under vacuum would greatly reduce these effects.

B. Plume-surface experiment

The radar interferometer was used to measure the concentration of the ejecta cloud generated by the thruster at a height of 15 cm above the granular surface. The measurement path is located across the bed diameter, at a height of 9 cm above the surface. The granular bed is kept uncompacted by emptying and refilling between each test. Measurements were conducted at pressures of 800 and 6.7 Pa, reproducing the martian and lunar environments respectively. A Chronos 1.4 high-speed camera was used to acquire footage of the impingement at 1057 frames per second to complement the results obtained by the radar. This measurement plan aims at demonstrating the instrument's capability to measure dense particle clouds without saturating, which will be expanded into a tomographic multi-reflector system in future studies. Times are reported from the initial impact of the jet on the granular bed, which is defined as the instant when the phase shift exceeds twice the standard deviation $\sigma_{\text{rnf}} = 0.14^\circ$ of the radar noise floor, indicating the onset of a large-scale disturbance. The PID results collected in the martian and lunar cases are presented in Fig. 12 with the 95% margin of error resulting from the instrument calibration shown as the shaded area around each traces. In either cases, the interferometer signal did not require phase unwrapping and its strength varied by less than 15% during the pulse duration.

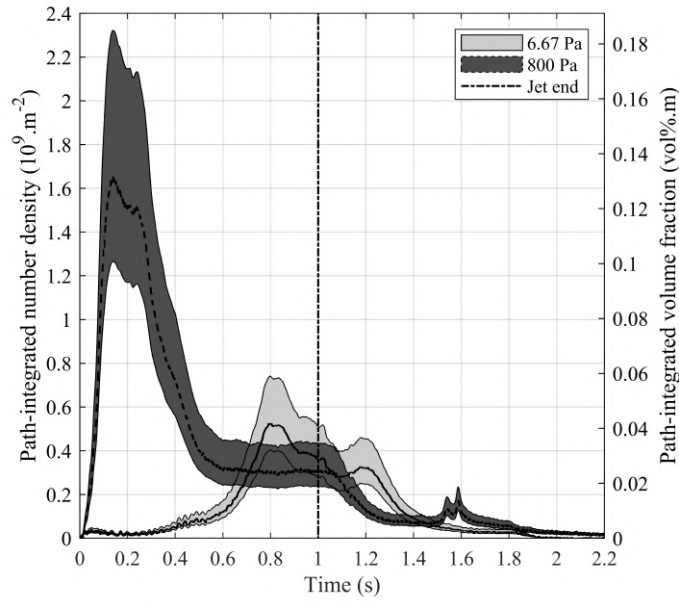


Fig. 12 Path-integrated ejecta densities across the nozzle axis at martian (800 Pa) and lunar (6.67 Pa) ambient pressures, for a radar-reflector distance of 58 cm.

1. Martian case (800 Pa)

In the martian case, the initial impingement creates a large surge of surface material, which reaches a maximum PID of $1.65 \pm 0.67 \times 10^9 \text{ particles.m}^{-2}$ 141 ms after the impact of the jet on the surface. The PID then reaches a steady-state value of $0.30 \pm 0.12 \times 10^9 \text{ particles.m}^{-2}$ that extends between 602 ms and 1073 ms. After 1073 ms, the thruster stops firing, and the PID decreases, except for a double surge at 1537 and 1586 ms with amplitudes of $0.14 \pm 0.04 \times 10^9 \text{ particles.m}^{-2}$ and $0.17 \pm 0.05 \times 10^9 \text{ particles.m}^{-2}$. The post-jet double surge can be explained by the settling of material previously ejected upward. These observations are confirmed by the video footage presented in Fig. 13 showing the large amount of ejecta generated in the initial phase of the impingement, followed by a less dense steady-state cloud, then material falling down after jet extinction. In particular, the footage reveals that most of the material in the initial ejecta peak is lifted in the first 35 ms after the initial impingement, with the maximum PID observed when this initial surge falls back to the ground. The initial ejecta surge appears to be due to a localized instance of soil liquefaction. This interpretation is suggested by the presence of erupting voids in the initial ejecta surge, as seen in Fig. 14. Pulsed landing thrusters, which generate such transients many times per second, were experimentally observed by Mehta et al. to dramatically increase erosion rates compared to a continuously-fired thruster, giving rise to

a new class of erosion phenomena called diffusive gas explosive erosion (DGEE) through the repeated application of this initial jet transient on an already fluidized surface [32]. On the other hand, prior work by Metzger [4] suggests that the steady-state erosion state observed later in the impingement is dominated by bearing capacity failure (BCF) and diffusion-driven-flow (DDF), with the crater and ejecta cloud being in granular flux equilibrium through the recirculation of ejecta falling back to the crater.

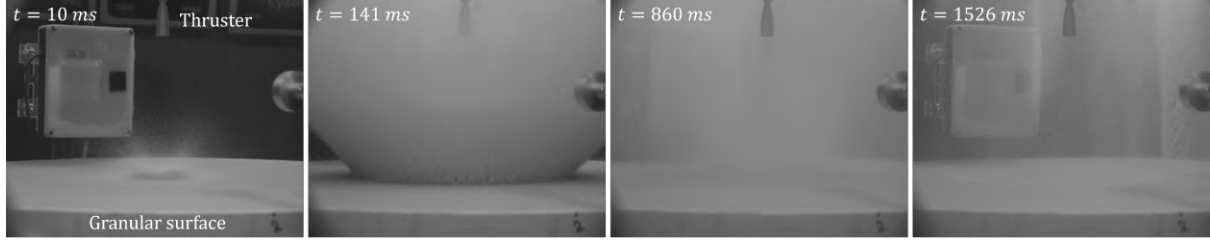


Fig. 13 Images of the jet impingement at 800 Pa, showing the initial particle spray ($t = 10\text{ms}$), maximum ejecta density ($t = 147\text{ms}$), steady-state density ($t = 860\text{ms}$), and particles falling from chamber ceiling after jet extinction ($t = 1526\text{ms}$).

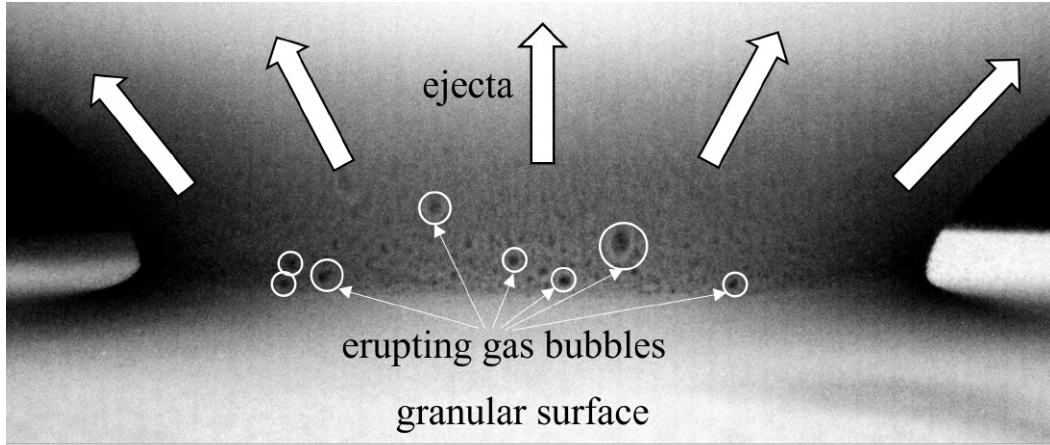


Fig. 14 Contrast-enhanced detail of ejecta surge at 800 Pa showing erupting gas bubbles, which suggests the occurrence of soil liquefaction.

Fig.12 shows a post-jet hysteresis with an amplitude of $1.5 \pm 0.5 \times 10^7 \text{ particles.m}^{-2}$, or 5% of the steady-state PID value, without a clear cause being currently identified. While particles falling back to the bed several seconds after the jet are visible in Fig. 13, it is unlikely that this phenomenon is responsible for this hysteresis, as the standard deviation of the post-jet phase signal is identical to the pre-jet noise floor. It is possible that a secondary propagation path involving a reflection on the particle bed was disturbed by the crater formation. The relative amplitude of this propagation path would be expected to be small with respect to the line-of-sight path between the radar and the reflector, because it is outside of the 2nd Fresnel zone. Improving the collimation of the radar beam, for example by adding a dielectric lens ahead of the antenna array, could help solve this issue.

2. Lunar case (6.67 Pa)

The lunar case is distinct from the martian case. First, there is no initial density peak: the PID shows a sharp but limited initial increase to $0.04 \pm 0.01 \times 10^9 \text{ particles.m}^{-2}$, a slow decrease until 172 ms, and then a gradual rise until 792 ms, reaching a peak of $0.52 \pm 0.22 \times 10^9 \text{ particles.m}^{-2}$. The PID then steadily decreases until 1103 ms to reach a value of $0.28 \pm 0.12 \times 10^9 \text{ particles.m}^{-2}$, with a slight increase to $0.33 \pm 0.14 \times 10^9 \text{ particles.m}^{-2}$ at 1180 ms, and then finally returning to the noise floor at 1950 ms.

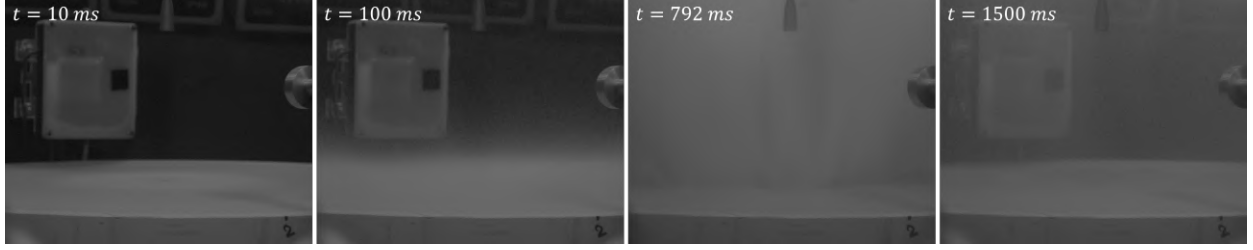


Fig. 15 Images of the jet impingement at 6.67 Pa, showing the initial jet impingement ($t = 10\text{ms}$), growing ejecta cloud without streaks ($t = 100\text{ms}$), maximum density ($t = 792\text{ms}$) with vertical streaks, and particles falling back after jet extinction ($t = 1500\text{ms}$).

The images presented in Fig. 15 confirm the absence of an initial surge of ejecta in the lunar case. Rather, particles are emitted from a large area at a relatively modest flux, creating a steadily densifying cloud of lofted particles. Then, at 310 ms, the formation of streaks, or tendrils, of ejectas is observed. Initially close to the ground, the streaks appear in the footage to become more and more vertical over the course of the pulse, until they are blown out and collapse at the end of the jet pulse, followed by the rest of the blown particles falling back to the bed. Fig. 16 shows the remains of these elongated structures emanating from the raised crater ridge created by the jet at 50 mTorr. Conversely, the crater generated by the jet at 800 Pa does not exhibit either a raised ridge or streak-like structures.

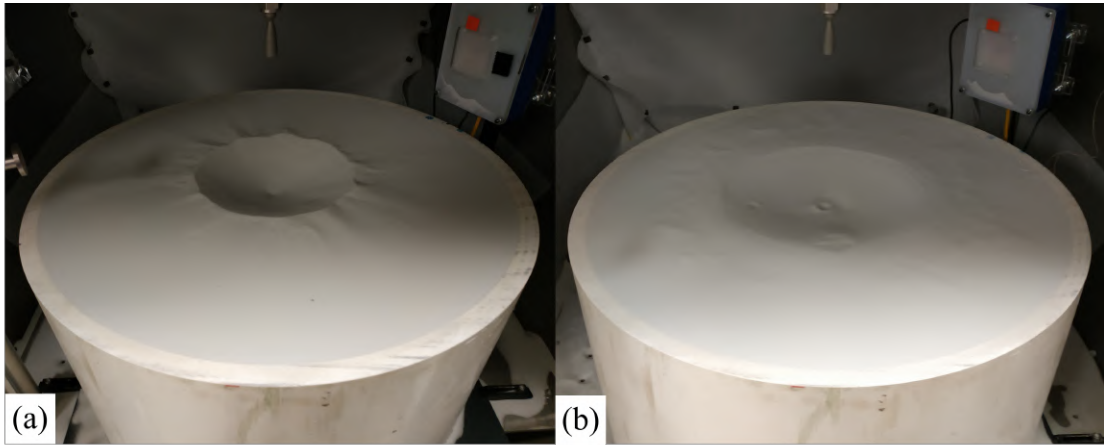


Fig. 16 Post-experiment craters obtained for an ambient pressure of 6.67 Pa (a), showing streak-like structures emanating from the crater ridge, and 800 Pa (b), where those structures are absent.

The large erosion area visible in the footage, as well as the combination of low ground pressure, moderate ejecta angle and low erosion rate, suggest that viscous erosion (VE) is the dominant erosion mechanism in the first phase of the lunar case. However, the increase in ambient pressure during the firing, which decreases the JPR from 340 initially to 15 on shutdown, combined with the formation of the crater, could lead to a shift from VE to a combined BCF and DDF erosion mode, which is supported by the increase in ejecta angle up to the vertical as well as the abrupt change in the slope of the PID measurements at 792 ms.

V. Conclusion

A millimeter-wave interferometer for ejecta density measurement has been developed, calibrated, and demonstrated at ambient pressures relevant to plume-surface interactions on the Moon and Mars. The instrument acquired quantitative, high-frequency path-integrated ejecta density measurements in conditions that blinded the concurrently-used optical camera. The calibration of the instrument yielded a phase-ejecta slope $\beta = 9.03 \pm 2.66^\circ \cdot 10^{-8} \text{ particles}^{-1} \cdot \text{m}^2$, with a coefficient of determination $r^2 = 0.9528$. In the martian case, the generation of a large surge of ejecta with a path-integrated density of $0.131 \pm 0.053 \text{ vol\%} \cdot \text{m}$ ($1.65 \pm 0.67 \times 10^9 \text{ particles} \cdot \text{m}^{-2}$) has been observed as well as the

establishment of a steady-state ejecta density of $0.0242 \pm 0.0097 \text{ vol\%.m}$ ($0.304 \pm 0.122 \times 10^9 \text{ particles.m}^{-2}$). The initial surge and steady-state surge are attributed to diffusive gas explosive erosion and a combination of bearing capacity failure and diffusion driven flow respectively. In the lunar case, the absence of initial ejecta surge, the progressive densification of the ejecta cloud up to a value of $0.0419 \pm 0.0170 \text{ vol\%.m}$ ($0.527 \pm 0.214 \times 10^9 \text{ particles.m}^{-2}$), and a likely transition from viscous erosion to bearing capacity failure-diffusion driven flow have been observed. Future works will expand on the current study by conducting the calibration process of the instrument under vacuum, thereby considerably improving its accuracy, as well as performing a multi-chord ejecta density measurement that will provide a time-resolved tomographic reconstruction of the ejecta cloud generated by the impingement of the thruster on the granular surface. The instrument can be applied to many opaque multiphase flow situations outside of planetary PSI, such as fluidized particle beds, rotorcraft brownouts, dust storms, combustion chambers flows, and smoke analysis.

VI. Acknowledgements

This work is supported by the National Aeronautics and Space Administration (NASA) under Grant No. 80NSSC20K0304 issued through the Early Stage Innovation Program. We acknowledge the contributions of Dr. Danehy, NASA Research Collaborator, through fruitful comments and discussions. We also thank Professor Bernhard from the Department of Electrical and Computer Engineering at the University of Illinois at Urbana-Champaign (UIUC) for her helpful suggestions and remarks regarding the instrument concept, the Visualisation Laboratory at UIUC for their material support in the development of the particle shadow counting system, the UIUC Aerospace Machine Shop for manufacturing many pieces of experimental hardware, as well as Professor Panerai and graduate student Cutler Philippe for their guidance in the implementation of the microCT technique for particle size measurement.

References

- [1] Immer, C., Metzger, P., Hintze, P. E., Nick, A., and Horan, R., "Apollo 12 Lunar Module exhaust plume impingement on Lunar Surveyor III," *Icarus*, Vol. 211, No. 2, 2011, pp. 1089–1102. <https://doi.org/https://doi.org/10.1016/j.icarus.2010.11.013>, URL <https://www.sciencedirect.com/science/article/pii/S001910351000432X>.
- [2] Immer, C., Lane, J., Metzger, P., and Clements, S., "Apollo video photogrammetry estimation of plume impingement effects," *Icarus*, Vol. 214, No. 1, 2011, pp. 46–52. <https://doi.org/https://doi.org/10.1016/j.icarus.2011.04.018>, URL <https://www.sciencedirect.com/science/article/pii/S0019103511001539>.
- [3] Wagner, S. A., "The Apollo experience lessons learned for constellation lunar dust management," *NASA Technical Publication TP-2006-213726*. Washington, DC: National Aeronautics and Space Administration, 2006.
- [4] Metzger, P. T., Immer, C. D., Donahue, C. M., Vu, B. T., Latta III, R. C., and Deyo-Svendsen, M., "Jet-induced cratering of a granular surface with application to lunar spaceports," *Journal of Aerospace Engineering*, Vol. 22, No. 1, 2009, pp. 24–32.
- [5] Metzger, P., Li, X., Immer, C., and Lane, J., "ISRU Implications for Lunar and Martian Plume Effects," *47th AIAA Aerospace Sciences Meeting including The New Horizons Forum and Aerospace Exposition*, 2009. <https://doi.org/10.2514/6.2009-1204>, URL <http://dx.doi.org/10.2514/6.2009-1204>.
- [6] Watkins, R., Metzger, P. T., Mehta, M., Han, D., Prem, P., Sibille, L., Dove, A., Jolliff, B., Moriarty III, D. P., Barker, D. C., Patrick, E., Kuhns, M., Laine, M., and Radley, C. F., "Understanding and Mitigating Plume Effects During Powered Descents on the Moon and Mars," *Bulletin of the AAS*, Vol. 53, No. 4, 2021. <https://doi.org/10.3847/25c2cfef.f9243994>, URL <https://baas.aas.org/pub/2021n4i089>.
- [7] Lane, J. E., and Metzger, P. T., "Estimation of Apollo Lunar Dust Transport using Optical Extinction Measurements," *Acta Geophysica*, Vol. 63, No. 2, 2015, pp. 568–599. <https://doi.org/10.1515/acgeo-2015-0005>, URL <https://doi.org/10.1515/acgeo-2015-0005>.
- [8] Lane, J. E., Mantovani, J. G., Mueller, R. P., Nugent, M. W., Nick, A. J., Schuler, J. M., and Townsend, I. I., *Optical Extinction Measurements of Dust Density in the GMRO Regolith Test Bin*, 2016, pp. 36–47. <https://doi.org/10.1061/9780784479971.005>, URL <https://ascelibrary.org/doi/abs/10.1061/9780784479971.005>.
- [9] Metzger, P. T., Dove, A., Conroy, M., Gloria, J., O'Reilly, A., and St. John, A., "Ejecta Sheet Tracking, Opacity, and Regolith Maturity (Ejecta Storm): An Instrument for Lunar Landing Plume Effects and Dust Dynamics," *Lunar and Planetary Science Conference*, 2021, p. 2616.

- [10] Ahmad, A., Roh, J. C., Wang, D., and Dubey, A., "Vital signs monitoring of multiple people using a FMCW millimeter-wave sensor," *2018 IEEE Radar Conference (RadarConf18)*, 2018, pp. 1450–1455. <https://doi.org/10.1109/RADAR.2018.8378778>.
- [11] Anitori, L., de Jong, A., and Nennie, F., "FMCW radar for life-sign detection," *2009 IEEE Radar Conference*, IEEE, 2009, pp. 1–6.
- [12] Mostov, K., Liptsen, E., and Boutchko, R., "Medical applications of shortwave FM radar: Remote monitoring of cardiac and respiratory motion," *Medical physics*, Vol. 37, No. 3, 2010, pp. 1332–1338.
- [13] Wang, G., Munoz-Ferreras, J.-M., Gu, C., Li, C., and Gomez-Garcia, R., "Application of linear-frequency-modulated continuous-wave (LFMCW) radars for tracking of vital signs," *IEEE transactions on microwave theory and techniques*, Vol. 62, No. 6, 2014, pp. 1387–1399.
- [14] Och, A., Hölzl, P. A., Schuster, S., Scheiblhofer, S., Zankl, D., Pathuri-Bhuvana, V., and Weigel, R., "High-Resolution Millimeter-Wave Tomography System for Nondestructive Testing of Low-Permittivity Materials," *IEEE Transactions on Microwave Theory and Techniques*, Vol. 69, No. 1, 2021, pp. 1105–1113. <https://doi.org/10.1109/TMTT.2020.3030662>.
- [15] An, S., He, Z. S., Li, J., An, J., and Zirath, H., "Micrometer accuracy phase modulated radar for distance measurement and monitoring," *IEEE Sensors Journal*, Vol. 20, No. 6, 2019, pp. 2919–2927.
- [16] Ayhan, S., Thomas, S., Kong, N., Scherr, S., Pauli, M., Jaeschke, T., Wulfsberg, J., Pohl, N., and Zwick, T., "Millimeter-wave radar distance measurements in micro machining," *2015 IEEE Topical Conference on Wireless Sensors and Sensor Networks (WiSNet)*, 2015, pp. 65–68. <https://doi.org/10.1109/WISNET.2015.7127413>.
- [17] Scherr, S., Göttel, B., Ayhan, S., Bhutani, A., Pauli, M., Winkler, W., Scheytt, J. C., and Zwick, T., "Miniaturized 122 GHz ISM band FMCW radar with micrometer accuracy," *2015 European Radar Conference (EuRAD)*, 2015, pp. 277–280. <https://doi.org/10.1109/EuRAD.2015.7346291>.
- [18] Pauli, M., Göttel, B., Scherr, S., Bhutani, A., Ayhan, S., Winkler, W., and Zwick, T., "Miniaturized millimeter-wave radar sensor for high-accuracy applications," *IEEE Transactions on Microwave Theory and Techniques*, Vol. 65, No. 5, 2017, pp. 1707–1715.
- [19] Tudisco, O., Lucca Fabris, A., Falcetta, C., Accatino, L., De Angelis, R., Manente, M., Ferri, F., Florean, M., Neri, C., Mazzotta, C., et al., "A microwave interferometer for small and tenuous plasma density measurements," *Review of Scientific Instruments*, Vol. 84, No. 3, 2013, p. 033505.
- [20] Akhtar, K., Scharer, J. E., Tysk, S. M., and Kho, E., "Plasma interferometry at high pressures," *Review of Scientific Instruments*, Vol. 74, No. 2, 2003, pp. 996–1001.
- [21] Domier, C., Peebles, W., and Luhmann Jr, N., "Millimeter-wave interferometer for measuring plasma electron density," *Review of Scientific Instruments*, Vol. 59, No. 8, 1988, pp. 1588–1590.
- [22] Lu, X. P., and Laroussi, M., "Electron density and temperature measurement of an atmospheric pressure plasma by millimeter wave interferometer," *Applied Physics Letters*, Vol. 92, No. 5, 2008, p. 051501.
- [23] Schulz, C., Baer, C., and Fiebrandt, M., "Millimeter Wave Radar-based Plasma Measurements," *2019 IEEE Asia-Pacific Microwave Conference (APMC)*, 2019, pp. 756–758. <https://doi.org/10.1109/APMC46564.2019.9038885>.
- [24] Porte, L., Rettig, C., Peebles, W., and Ngyuen, X., "Design and operation of a low cost, reliable millimeter-wave interferometer," *Review of scientific instruments*, Vol. 70, No. 1, 1999, pp. 1082–1084.
- [25] Markel, V. A., "Introduction to the Maxwell Garnett approximation: tutorial," *Journal of the Optical Society of America A*, Vol. 33, No. 7, 2016, pp. 1244–1256. <https://doi.org/10.1364/JOSAA.33.001244>, URL <http://josaa.osa.org/abstract.cfm?URI=josaa-33-7-1244>.
- [26] "MiePlot," , 2021. URL <http://www.philiplaven.com/mieplot.htm>.
- [27] *AWR6843 Single-Chip 60- to 64-GHz mmWave Sensor*, Texas Instruments, 2020. URL <https://www.ti.com/lit/ds/symlink/awr6843.pdf>, rev. C.
- [28] *DCA1000EVM Data Capture Card*, Texas Instruments, 2018. URL <https://www.ti.com/lit/ug/spruij4a/spruij4a.pdf>, rev. A.
- [29] *Photron FASTCAM SA-Z*, PHOTRON LIMITED, 2013. URL <https://photron.com/fastcam-sa-z-2/>.
- [30] Al-Rashdan, H., "Supersonic Underexpanded Flow Visualization in Sub-Atmospheric Facility," *AIAA AVIATION 2021 FORUM*, 2021. <https://doi.org/10.2514/6.2021-2859>, URL <https://arc.aiaa.org/doi/abs/10.2514/6.2021-2859>.

- [31] Letz, M., *Microwave Dielectric Properties of Glasses and Bulk Glass Ceramics*, John Wiley & Sons, Ltd, 2017, Chap. 7, pp. 345–354. <https://doi.org/https://doi.org/10.1002/9781119208549.ch7>, URL <https://onlinelibrary.wiley.com/doi/abs/10.1002/9781119208549.ch7>.
- [32] Mehta, M., Renno, N. D. O., Marshall, J. R., Grover, M. R., Sengupta, A., Rusche, N. A., Kok, J. F., Arvidson, R. E., Markiewicz, W. J., Lemmon, M. T., and Smith, P. H., “Explosive erosion during the Phoenix landing exposes subsurface water on Mars,” *Icarus*, Vol. 211, 2011, pp. 172–194.